J Mater Sci: Mater Med (2011) 22:1625–1631
DOI 10.1007/s10856-011-4339-y

Microwave-assisted rapid discharge sintering of a bioactive glass–ceramic

Kevin P. O'Flynn · Barry Twomey · Aidan Breen · Denis P. Dowling · Kenneth T. Stanton

Received: 23 March 2011 / Accepted: 4 May 2011 / Published online: 15 May 2011

Abstract Bioactive glass–ceramics have been developed as successful bone graft materials. Although conventional sintering in an electrically-heated furnace is most commonly used, an alternative microwave plasma batch processing technique, known as rapid discharge sintering (RDS), is examined to crystallise the metastable base glass to form one or more ceramic phases. Apatite-mullite glass–ceramics (AMGC) were examined to elucidate the effects of RDS on the crystallization of a bioactive glass–ceramic. By increasing the fluorine content of the glass, the fluorapatite (FAp) and mullite crystallization onset temperatures can be reduced. Samples were sintered in a hydrogen and hydrogen/nitrogen discharge at temperatures of $\approx$800 and 1000°C respectively with the higher sintering temperature required to form mullite. Results show that the material can be densified and crystallised using RDS in a considerably shorter time than conventional sintering due to heating and cooling rates of $\approx$400°C/min.

1 Introduction

Glass–ceramics are metastable glasses that, when heat-treated, crystallise to form ceramics. Bioactive glass–ceramics have been developed as an alternative to synthetic hydroxyapatite ($Ca_{10}(PO_4)_6(OH)_2$, HA) for use in vivo both in restorative dental applications and bone implantation [1]. Bioactive glasses and glass–ceramics have been shown to be more biocompatible than metals or fine ceramics [2]. They can be produced with little or no porosity, have a reproducible fine-grained microstructure and can have mechanical and bioactivity properties tailored to specific applications [3, 4]. Such ceramics can be used as cast dental implants or as enamelled coatings for orthopaedic implants [5–7].

There are several important bioactive glass–ceramic systems and examples include apatite-wollastonite [8], mica-based [9, 10] and apatite-mullite [11, 12]. During the sintering of wollastonite- and mica-containing glass–ceramics, either slow heating rates or extended hold times at elevated temperatures are recommended in order for the glass to become optimally crystalline [8]. Apatite–mullite glass–ceramics (AMGC) are examined here as they can be crystallized using a high heating rate and do not require a hold time to crystallize [4, 13]. This makes them suitable for use in conjunction with rapid sintering techniques such as microwave, plasma, electrical discharge and laser sintering [14]. The benefits of microwave sintering include significantly faster heating rates over conventional methods as well as reduced grain sizes and increased sintered-body density at lower sintering temperatures [14, 15]. As well as higher heating rates, microwave sintering offers improved mechanical properties due to finer microstructures achieved at equivalent sintering temperatures to conventional resistance heating [15, 16]. As well as for their use with metals, non plasma microwaves have been successfully used to sinter ceramics [17, 18]. Agrawal et al. [17] demonstrated that microwave sintering of HA produced higher densities than conventional sintering in significantly shorter times (10 min of microwave sintering at 1200°C compared to 120 min at 1300°C for conventional sintering).

The use of microwave plasma sintering was first proposed in 1968 by Bennett [19]. In microwave sintering

K. P. O'Flynn · B. Twomey · A. Breen · D. P. Dowling · K. T. Stanton (✉)
School of Mechanical and Materials Engineering, University College Dublin, Belfield, Dublin 4, Ireland
e-mail: kenneth.stanton@ucd.ie

systems, plasma or arc discharges are common occurrences due to the use of a partial vacuum, a controlled atmosphere (typically hydrogen, nitrogen or argon) and a high powered electrical source [20]. These discharges are traditionally avoided, as a non-uniform discharge may result in hot spots on the sample edges producing inhomogeneous heating. Bennett [19] however, demonstrated that through the formation of a controlled plasma discharge, uniform sintering could be achieved when the sintered body is placed inside the plasma discharge.

A microwave-assisted plasma is formed when an electromagnetic field of sufficient strength excites the surrounding gas enough to cause the atoms to separate into electrons and positive ions via elastic and inelastic collisions [21, 22]. This is more readily achieved under vacuum and in the presence of specific gases. In general, smaller atomic weight gases (e.g. hydrogen) will more readily form a plasma due to their higher ionisation potential, while higher atomic weight gases (e.g. nitrogen) will form hotter plasmas as a result of resistance due to their lower ionisation potential [23, 24]. In the case of rapid discharge sintering (RDS), a plasma ball induced by microwave energy is formed in the centre of the chamber. The heat generated by the plasma is used to directly heat samples placed in the discharge. Due to the localised heating effect of the plasma the surrounding chamber remains relatively cool, thus facilitating substrate heating and cooling rates of up to $\approx$400°C/min [25]. This is in contrast to conventional resistive furnace heating, which require lengthy heating/cooling times or high energies due to the requirement to heat and cool the chamber surrounding the samples. To-date there has been a number of reports on the sintering of metal powders [26, 27] using plasma microwave but sintering of ceramic materials has been limited to alumina [19, 28, 29]. The work presented in this paper aims to determine the feasibility of using the RDS process for sintering of small batches of bioactive glass–ceramics for possible use in dental implants such as inlays.

2 Materials and methods

2.1 Glass synthesis

The particular AMGC system used has a generic composition of $1.5(5 - x)\cdot SiO_2$–$(5 - x)\cdot Al_2O_3$–$1.5P_2O_5$–$(5 - x)\cdot CaO$–$xCaF_2$, where x can vary between 1.0 and 2.5. This system has previously been examined with detailed thermal and X-ray analysis and is designed to maintain an apatitic Ca:P ratio of 1.67 [4, 13]. The fluorine acts as a network modifier, increasing atomic mobility, and lowering the glass transition and crystallization temperatures [30]. Using glasses with different fluorine contents produces glasses with a wide range of crystallization temperatures. This will allow a glass composition to be identified that is optimised for use with RDS.

To make the glass, the reagents were mixed for 40 min in a ball mill without P_2O_5 due to the hygroscopic nature of the latter component. The P_2O_5 was then added and the mixture ball-milled for a further 15 min. The mixed powder was placed into a high-density lidded mullite crucible. Using a conventional electric furnace, the crucible and charge were heated to the firing temperature shown in Table 1 and held at this temperature for 2 h. The glass melt was then poured directly into demineralised water to shock quench it to room temperature, thereby avoiding crystallization and preserving the amorphous nature of the glass. The resultant glass was oven dried in air for 1 day. Once dry, it was crushed and sieved to <45 μm. To make disks suitable for sintering, 0.25 g of <45 μm powder was pressed, without binder, for 20 s at 40 bar in 12.8 mm diameter die to form a disk.

2.2 Rapid discharge sintering

The RDS processing was carried out using a circumferential antenna plasma (CAP) microwave system (Fig. 1) as described in more detail elsewhere [31]. Disc samples were sintered either in a hydrogen or hydrogen and nitrogen plasma at a pressure of 20 mbar. For samples processed with hydrogen alone, the gas flow rate was maintained at 150 sccm for these samples and the final resultant treatment temperature was approximately $\approx$800°C, as measured using a two-colour pyrometer [32]. In order to obtain a higher firing temperature, 30 sccm of nitrogen was added to the hydrogen gas, while keeping the other operating conditions constant. It has been reported previously that the addition of larger atomic weight diatomic gases increases plasma sintering temperatures [23] and under these conditions, sintering temperatures of $\approx$1000°C have been observed [32]. The green body discs were rotated in the plasma ball (diameter approximately 5 cm) located at the centre of the CAP chamber at a rotation speed of 1 rpm. Input powers of up to 3 kW were supplied from a 6 kW

Table 1 Glass codes, firing and crystallization temperatures of glasses (from DSC)

Glass code	x Value	Firing temperature (°C)	T_g (°C)	T_{p1} (°C)	T_{p2} (°C)
G250	2.50	1420	629	682	833
G200	2.00	1420	650	755	961
G175	1.75	1430	676	836	1032
G150	1.50	1440	696	917	1073
G100	1.00	1440	726	1036	1121

Muegge microwave power supply operating at 2.45 GHz. Sample temperatures were measured using a LASCON QP003 two-colour pyrometer (Dr. Merganthaler GmBH and Co, Ulm, Germany). The use of a two-colour pyrometer is expected to eliminate the interference effect of the plasma on the emissivity of the sample as no significant plasma emissions are observed for hydrogen and nitrogen at the operating wavelengths of the pyrometer (1.68 and 1.916 μm) [32]. Rapid heating and cooling rates of >300°C/min were observed in the microwave plasma fired samples.

2.3 Material physicochemical characterisation

Differential scanning calorimetry (DSC) was performed on the <45 μm powder using a Rheometric Scientific STA 1500 (Surrey, UK) to determine the glass transition temperature (T_g) and peak crystallization temperatures (T_p) of the different glass compositions. A flowing dry nitrogen atmosphere with a heating rate of 10°C/min was used with matched platinum–rhodium crucibles. Samples were heated between room temperature and 1200°C.

Powder XRD was used to confirm that the glass was initially fully vitreous and then to identify phases present in the sintered body. Analysis was carried out in a Huber 642 Guinier Diffractometer (Rimsting, Germany) with a quartz Johansson monochromator and copper target operating in subtractive transmission mode at 40 kV and 30 mA. X-rays were pure monochromatic Cu Kα_1 with $\lambda = 1.54056$ Å. A Fuji ImagePlate was used to collect the pattern after a 10 min exposure with 10 scan loops. Si powder (pure element grade, 99.5% pure, Johnson Matthey Alfa Products, Karlsruhe, Germany) was added at 10 wt% to samples as an internal standard to allow correction for non-linear peak shift. JCPDS powder diffraction file card 00-015-0776 was used to identify mullite and 00-015-0876 for fluorapatite (FAp). Lattice parameters were calculated using the method of Holland and Redfern [33]. The lattice parameters were refined using *d*-spacings. The size (τ) of the FAp crystals was determined from the (211) peak, which corresponds to 100% peak intensity, using the Scherrer equation [34]:

$$\tau = \frac{K\lambda}{B\cos(\theta)} \quad (1)$$

where K is the Scherrer constant, typically 0.9, λ is the wavelength of the incident X-rays, B is the full width at half maximum of the peak in radians, and θ is the Bragg angle in radians also. To determine B and θ, a Gaussian curve was fitted to the peak using a least sum of squares refinement. Here it is assumed that the line broadening does not occur due to stresses within the crystals [35].

A Hitachi TM-1000 scanning electron microscope (SEM) was used to examine the samples before and after sintering.

3 Results and discussion

3.1 Characterisation of the glass

XRD was used to show that each of the starting powders was a glass with no crystallinity evident (see Fig. 2). DSC was used to determine the thermal processing characteristics of the powders. Each of the glasses displayed a distinct glass transition temperature, T_g, and two exotherms corresponding to crystallization of FAp ($Ca_{10}(PO_4)_6F_2$) at T_{p1} and the simultaneous crystallization of mullite ($Si_2Al_3O_{13}$) and FAp at T_{p2} [5]: these are listed in Table 1.

As the fluorine content increases, the crystallization temperatures decrease. Varying levels of fluorine allow the

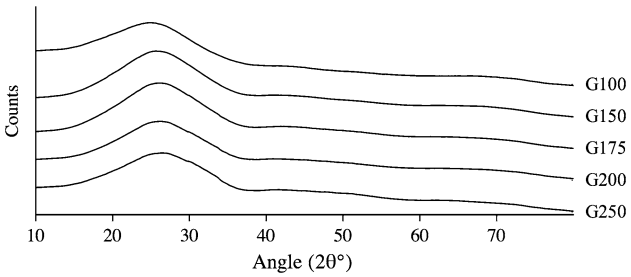

Fig. 2 XRD of the different glasses prior to sintering. The amorphous halo characteristic of the disordered structure in glass is clearly evident

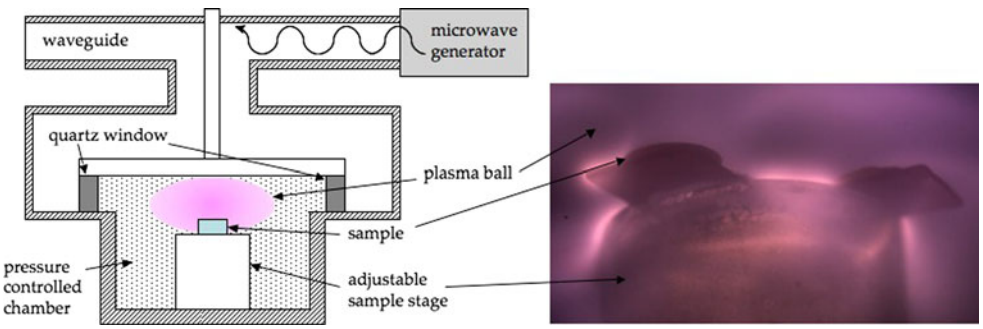

Fig. 1 Schema of the RDS system (*left*) with a photograph of the plasma inside the chamber (*right*)

effect of different glass crystallization temperatures subjected to different RDS parameters to be investigated.

3.2 RDS of the glasses in a hydrogen plasma

Based on previous studies with the CAP system, the use of a hydrogen atmosphere at 20 mbar pressure should yield substrate treatment temperatures of ≈800°C [32]. It can be postulated that only high fluorine glass samples will show any change in crystallinity at this temperature. Based on Table 1, only G175, G200, and G250 should crystallize at or below this temperature.

Each of the glass types were sintered at seven different power and time combinations in a hydrogen discharge and examined using XRD. The processing conditions and results are presented in Table 2 and graphed in Fig. 3.

After sintering, only FAp was found to have crystallised and, as expected, this phase was only observed in the high fluorine content samples, $x > 1.75$. Indeed the small and very broad peaks of G175 indicate that the temperature was just sufficient to crystallise the glass and only very small crystals of FAp were able to form. This is in good agreement with the measured sample temperature 798 ± 10°C which is just above the $T_{p1,\text{onset}}$ for the glass, which was 795°C from the DSC data (Fig. 4).

If the glass had been heated by the plasma to the second crystallization peak ($T_{p2,\text{onset}}$), which occurs at 810°C, one would expect to find the presence of mullite. However since there was no mullite found in G250, which has the lowest T_{p2}, it can be assumed that the scatter in the temperature measurement is an instrument error rather then a difference in sample temperature.

This indicates that the effective temperature in the hydrogen discharge was not sufficient for complete crystallization. The results show an interesting insight into the operation of RDS with glass samples: higher input powers and longer treatment times do not appear to increase the temperature of the samples, with the maximum operating temperature of ≈800°C remaining consistent for each of the processing conditions used. Upon inspection of the XRD data for G175, it is seen that despite increasing the power inputted to the RDS chamber by 1.8 kW, little increase in the crystallinity of the sample was observed. This demonstrates that changing the power does not significantly increase the final discharge temperature,

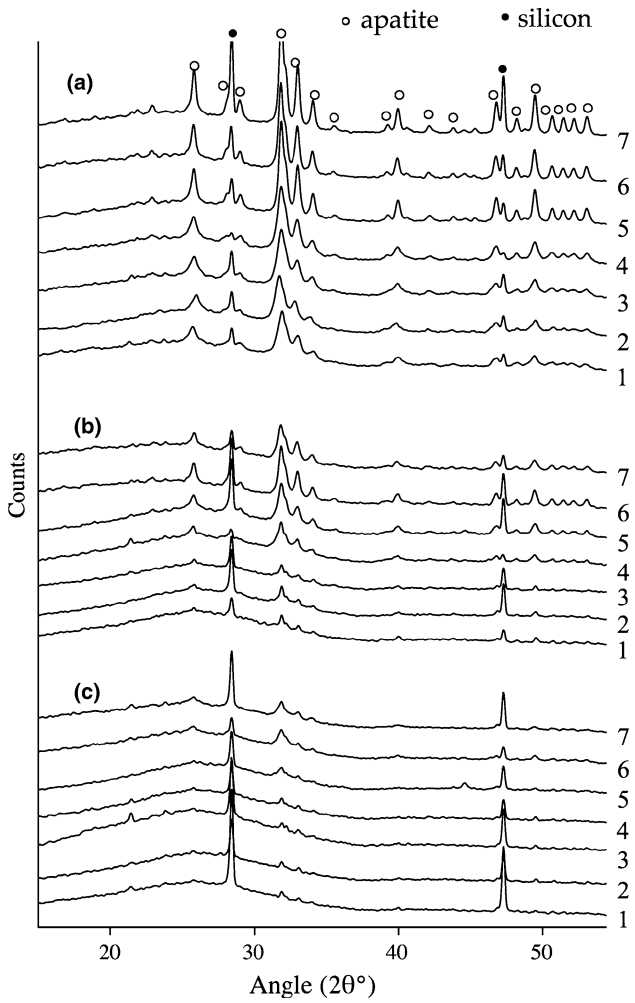

Fig. 3 XRD of **a** G250, **b** G200, **c** G175 showing the presence of apatite but not mullite. The sample codes are explained in Table 2. Silicon was used as an internal standard

Table 2 Phases crystallised after sintering, FAp and glass (G) in a hydrogen discharge

Sample number	Power (kW)	Hold time (min)	Phases present (XRD)				
			G250	G200	G175	G150	G100
1	1.8	3	FAp + G	FAp + G	FAp + G	G	G
2		10	FAp + G	FAp + G	FAp + G	G	G
3	2.4	3	FAp + G	FAp + G	FAp + G	G	G
4		10	FAp + G	FAp + G	FAp + G	G	G
5	3	3	FAp + G	FAp + G	FAp + G	G	G
6		10	FAp + G	FAp + G	FAp + G	G	G
7	2.4	30	FAp + G	FAp + G	FAp + G	G	G

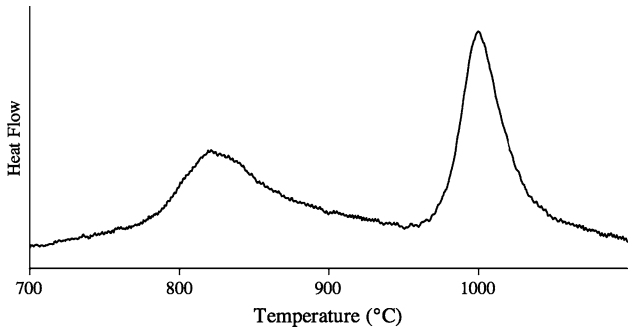

Fig. 4 DSC graph of G175 heated at 10°C/min. The two peaks correspond to the formation of apatite (T_{p1}) and apatite and mullite (T_{p2}). The onset of T_{p1} occurs at 795°C

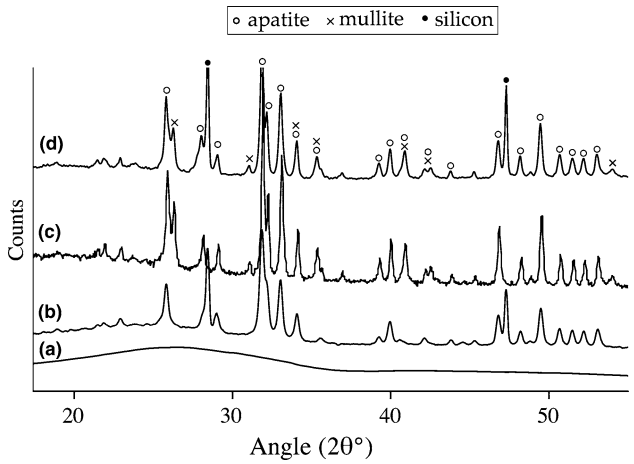

Fig. 5 XRD patterns of (*a*) G250 glass, (*b*) H_2 plasma sintered, (*c*) N_2/H_2 plasma sintered and (*d*) furnace sintered fully crystalline G250

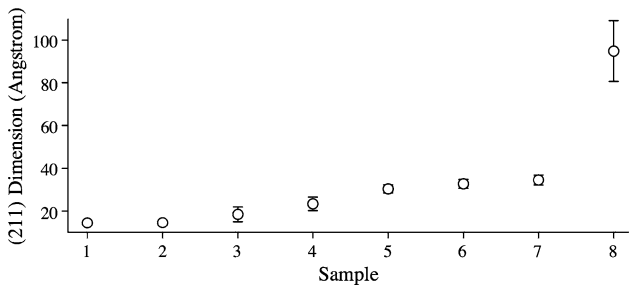

Fig. 6 Results of the Scherrer equation applied to the (211) diffraction plane for G250 sintered: (samples 1–7) in a hydrogen only discharge and (sample 8) in a hydrogen/nitrogen discharge. *Error bars* indicate 95% confidence

although the plasma ball increases from 5 to 10 cm in diameter and higher heating rates are observed using higher powers [25]. Longer soaks allow the crystallization more time to proceed, which has a greater effect on the crystallinity.

Little or no difference was observed between the sample temperatures of the glass–ceramics and, for example, nickel–diamond metal–matrix composites [32] under equivalent operating conditions. However, although increasing the plasma power increases the discharge size and heating rates, the maximum discharge temperature appears to be strongly dependant on the gas mixture. Once a uniform discharge is formed, samples placed in the discharge are heated directly by the plasma. This eliminates the necessity to use microwave transparent holders and susceptor heating typically used in non-plasma microwave sintering [15].

One concern was that RDS treatment could cause fluorine loss as silicon tetrafluoride (SiF_4) from the ceramic's surface due to the extremely high heating rates. This may result in a fluorine-deficient phase called anorthite [$CaAl_2Si_2O_8$] to form [11]. Upon inspection of the XRD results, no evidence of the unwanted formation of anorthite was found.

3.3 RDS of the glass in a hydrogen/nitrogen discharge

G250 was chosen for further testing as it had the lowest processing temperatures and exhibited the highest degree of FAp crystallization. Samples were prepared as before and during RDS nitrogen was added to the hydrogen discharge gas to increase the discharge temperature [25]. Samples were sintered at a maximum power of 2.4 kW with a 10 min dwell time. Using pryometry, the sample temperature was measured as 1,004 ± 11°C. Since this temperature is above T_{p2} for G250, mullite would be expected to form. As illustrated in Fig. 5, mullite is evident for samples sintered in the hotter hydrogen/nitrogen discharge and apatite and mullite can be formed at heating rates of ≈400°C/min. Compared to the times required to form FAp in other glass systems, this represents a significant process improvement.

The crystal sizes as determined by the Scherrer equation for the (211) plane of G250 are shown in Fig. 6. The crystal sizes show that the average crystal size increases with time. This indicates that the crystals are coarsening at longer times. When the hydrogen and nitrogen atmosphere is used, the apatite crystals become significantly larger, as expected. This results from apatite crystal growth and further crystallization during the second crystallization peak, as reported by Stanton et al. [36].

After sintering, the samples were broken in half and the fracture surfaces examined using SEM, see Fig. 7. The onset of particle necking was observed only in samples with x values ≥1.75, see Fig. 7b. This result was surprising as if one assumes, as is proposed here, that the processing temperature was ≈800°C then each of the G was above their respective T_g and would have been expected to undergo some level of viscous flow. Inspecting (Fig. 7a) it is clear that the particles retained their angular nature.

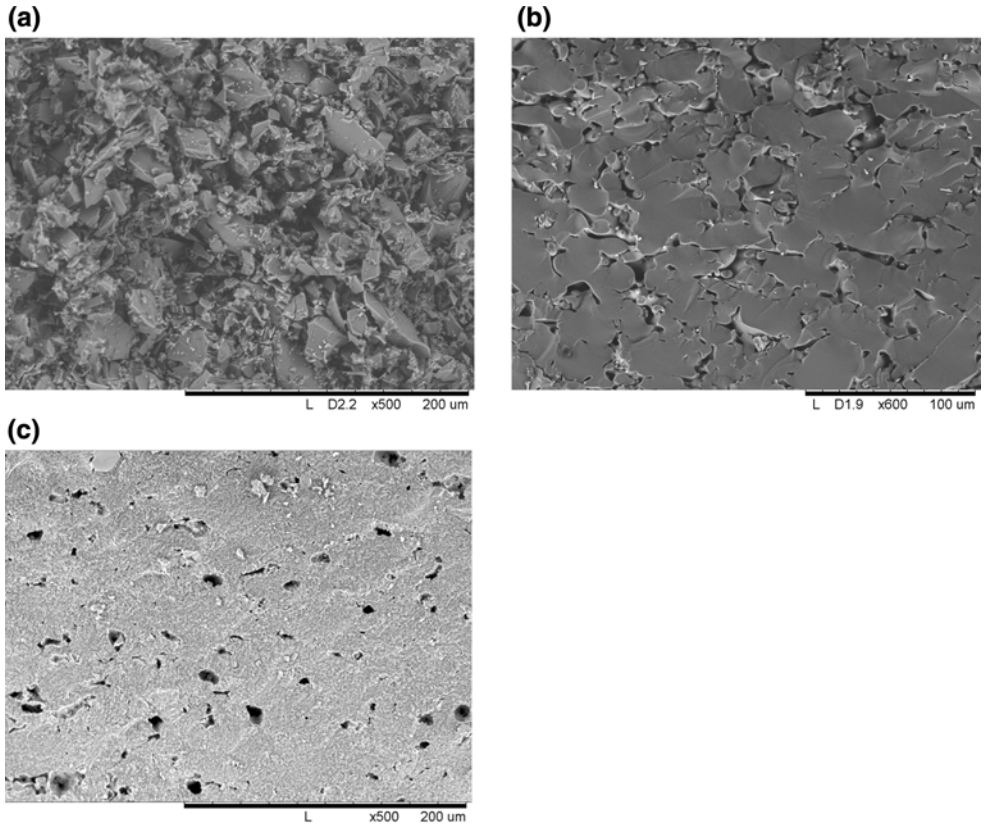

Fig. 7 SEM micrographs of **a** uncrystallized, **b** FAp crystallized and **c** FAp and mullite crystallized AMGC. **a** Shows sample 1 of G100, no bonding appears to have occurred; **b** shows the fracture surface of sample 6 of G175, particle necking was observed under these conditions. **c** Shows the fracture surface of G250 after sintering in a hydrogen/nitrogen plasma, densification has occurred

Inspecting Fig. 7b and c, obtained for G treated in a hydrogen atmosphere and a hydrogen/nitrogen atmosphere respectively, it can be seen that some densification has occurred compared with the uncrystallized glass (Fig. 7a). One possible reason for it not happening has previously been suggested by O'Flynn and Stanton [37]: particle bonding initially occurs at lower temperatures in high fluorine content glass because of a lower network connectivity. This lowers the viscosity of the glass and aids particle bonding. However, as crystallization of FAp proceeds, it depletes the fluorine in the local surrounding region of glass producing an accompanying increase in the network connectivity and this inhibits further particle bonding. It is only when the mullite begins to crystallise that the local residual glass network connectivity is lowered sufficient for bonding to continue. This could explain the lack of full densification of the FAp sample shown in Fig. 7b, despite the long dwell time.

4 Conclusions

Microwave-assisted RDS was successfully used to crystallise a bioactive glass–ceramic to form apatite and mullite. The required processing conditions were also identified. The high heating and cooling rates ($\approx$400°C/min) of RDS did not cause higher levels of fluorine-containing volatile evolution or the production of anorthite. XRD results suggest that the maximum temperature reached by the samples in a hydrogen discharge was just above T_{p1} onset for G175 which is 790°C and below the mullite crystallization onset temperature for G250 at 815°C but it was shown to produce apatite in glasses with $x_F \geq 1.75$. This in good agreement with the pyrometer measured sample temperature of 798 $\pm$ 10°C. Although these temperatures do not permit the crystallization of mullite, a hydrogen-only discharge is still useful if selective sintering of only the FAp phase is desired in conjunction with densification of powder samples. Particle necking and sintering was shown to occur in high fluorine glasses indicating that viscous flow did occur. Using a hydrogen/nitrogen atmosphere, the sample temperature increased to 1,004 $\pm$ 11°C, which was sufficient to form both apatite and mullite with little residual glass. Increasing the sintering time and plasma power resulted in an increase in the average crystal size of the FAp phase but this is thought to be due to longer soak times. At higher sintering temperatures with the hydrogen/nitrogen

atmosphere, a more significant increase in crystal size was observed due to further apatite crystallization and recrystallization. Samples treated in the hydrogen/nitrogen atmosphere were shown to obtain a greater density compared to hydrogen alone. The results indicate that RDS is a suitable method for the rapid production of devitrified AMGC.

References

1. Höland W. Biocompatible and bioactive glass-ceramics—state of the art and new directions. J Non-cryst Solids. 1997;219:192–7.
2. Moawad H, Jain H. Development of nano-macroporous soda-lime phosphofluorosilicate bioactive glass and glass-ceramics. J Mater Sci Mater Med. 2009;20(7):1409–18. doi:10.1007/s10856-009-3711-7.
3. Freeman CO, Brook IM, Johnson A, Hatton PV, Hill RG, Stanton KT. Crystallization modifies osteoconductivity in an apatite–mullite glass–ceramic. J Mater Sci Mater Med. 2003;14(11):985–90. doi:10.1023/a:1026306901058.
4. Stanton K, Hill R. The role of fluorine in the devitrification of $SiO_2{\cdot}Al_2O_3{\cdot}P_2O_5{\cdot}CaO{\cdot}CaF_2$ glasses. J Mater Sci. 2000;35(8):1911–6. doi:10.1023/a:1004710301219.
5. Stanton K, O'Flynn K, Nakahara S, Vanhumbeeck J-F, Delucca J, Hooghan B. Study of the interfacial reactions between a bioactive apatite–mullite glass–ceramic coating and titanium substrates using high angle annular dark field transmission electron microscopy. J Mater Sci Mater Med. 2009;20(4):851–7. doi:10.1007/s10856-008-3650-8.
6. Stanton KT, O'Flynn KP, Newcomb S. TEM study of the reaction interface between an apatite–mullite glass–ceramic and Ti6Al4V. Key Eng Mater. 2007;361–363:269–72. doi:10.4028/www.scientific.net/KEM.361-363.269.
7. Stanton KT, Vanhumbeeck JF. Bioactive apatite–mullite glass–ceramic coatings on titanium substrates. Adv Sci Technol. 2006;45:1275–80. doi:10.4028/www.scientific.net/AST.45.1275.
8. Kokubo T, Shigematsu M, Nagashima Y, Tashiro M, Nakamura T, Yamamuro T, Higashi S. Apatite- and wollastonite-containing glass–ceramics for prosthetic application. Bull Inst Chem Res Kyoto Univ. 1982;60:260–8.
9. Grossman DG (1974) Tetrasilicic mica glass–ceramic article. US Patent US3,839,055, 1 Oct 1974.
10. Beall G, Montierth M, Smith G. Machinable glass–ceramics. Microtecnic. 1972;26:173.
11. Clifford A, Hill R. Apatite–mullite glass–ceramics. J Non-cryst Solids. 1996;196:346–51.
12. Hill R, Wood D. Apatite–mullite glass–ceramics. J Mater Sci Mater Med. 1995;6(6):311–8. doi:10.1007/bf00120298.
13. Stanton KT, Hill RG. Crystallisation in apatite–mullite glass–ceramics as a function of fluorine content. J Cryst Growth. 2005;275(1–2):e2061–8.
14. Wroe R. Microwave sintering coming of age. Met Powder Rep. 1999;54(7/8):24–8.
15. Roy R, Agrawal D, Cheng J, Gedevanishvili S. Full sintering of powdered-metal bodies in a microwave field. Nature. 1999;399(6737):668–70.
16. Anklekar R, Bauer K, Agrawal D, Roy R. Improved mechanical properties and microstructural development of microwave sintered copper and nickel steel PM parts. Powder Metall. 2005;48(1):39–46.
17. Agrawal D, Fang Y, Roy D, Roy R. Fabrication of hydroxyapatite ceramics by microwave processing. Mater Res Soc Symp Proc. 1992;269:231–6.
18. Wroe FCR. Transferring microwave-assisted technology to the ceramic industry. MRS Proc. 1994;347:47–56. doi:10.1557/PROC-347-47.
19. Bennett CEG, McKinnon NA, Williams LS. Sintering in gas discharges. Nature. 1968;217(5135):1287–8.
20. Clark DE, Sutton WH. Microwave processing of materials. Annu Rev Mater Sci. 1996;26(1):299–331. doi:10.1146/annurev.ms.26.080196.001503.
21. Lieberman MA, Lichtenberg AJ. Principles of plasma discharges and materials processing. New York: Wiley-Blackwell; 2005.
22. Tan W, Grotjohn TA. Modelling the electromagnetic field and plasma discharge in a microwave plasma diamond deposition reactor. Diam Relat Mater. 1995;4(9):1145–54.
23. Lynn Johnson D, Sanderson W, Knowlton J, Kemer E, Chen M-Y. Advances in plasma sintering of alumina. Sci Sinter. 1988;20(2/3):109–13.
24. Roth JR. Industrial plasma engineering: principles. London: Taylor and Francis; 1995.
25. Breen A, Byrne G, Twomey B, Dowling D. Novel rapid discharge sintering technique for damage-free diamond metal matrix composites. Powder Metall. 2011;54(2):100–2.
26. Lourenço JM, Maliska AM, Klein AN, Muzart JLR. Plasma sintering of unalloyed iron: a study of surface porosity. Mater Res. 2004;7(2):269–75. doi:10.1590/S1516-14392004000200009.
27. Pavanati HC, Maliska AM, Klein AN, Muzart JLR. Comparative study of porosity and pores morphology of unalloyed iron sintered in furnace and plasma reactor. Mater Res. 2007;10(1):87–93. doi:10.1590/S1516-14392007000100019.
28. Lynn Johnson D, Sanderson W, Knowlton J, Kemer E, Chen M-Y. Advances in plasma sintering of alumina. Sci Sinter. 1988;20(2/3):109–13.
29. Page RA, Spooner S, Sanderson WB, Johnson D. Pore evolution during glow discharge sintering of alumina. J Am Ceram Soc. 1988;71(12):1125–9.
30. Ray NH. Inorganic polymers. London: Academic Press; 1978.
31. McConnell ML, Dowling DP, Pope C, Donnelly K, Ryder AG, O'Connor GM. High pressure diamond and diamond-like carbon deposition using a microwave CAP reactor. Diam Relat Mater. 2002;11:1036–40.
32. Twomey B, Breen A, Byrne G, Hynes A, Dowling DP. Rapid discharge sintering of nickel–diamond metal matrix composites. J Mater Process Technol. 2011;211(7):1210–16. doi:10.1016/j.jmatprotec.2011.02.002.
33. Holland T, Redfern S. Unit-cell refinement: changing the dependent variable, and use of regression diagnostics. Miner Mag. 1997;61:65–77.
34. Patterson A. The Scherrer formula for X-ray particle size determination. Phys Rev. 1939;56(10):978–82.
35. Bocker C, Rüssel C. Self-organized nano-crystallisation of BaF_2 from $Na_2O/K_2O/BaF_2/Al_2O_3/SiO_2$ glasses. J Eur Ceram Soc. 2009;29(7):1221–5.
36. Stanton KT, O'Flynn KP, Kiernan S, Menuge J, Hill R. Spherulitic crystallization of apatite–mullite glass–ceramics: mechanisms of formation and implications for fracture properties. J Non-cryst Solids. 2010;356(35–36):1802–13. doi:10.1016/j.jnoncrysol.2010.07.006.
37. O'Flynn KP, Stanton KT. Nucleation and early stage crystallization of fluorapatite in apatite–mullite glass–ceramics. Cryst Growth Des. 2010;10(3):1111–7. doi:10.1021/cg900868t.